

Laser-carbonized Electrodes on Implantable CMOS-based Imaging Device for Simultaneous Deep-brain Optical and Electrophysiological Measurements

Virgil Christian G. Castillo,¹ Kuang-Chih Tso,² Ryoma Okada,¹ Yasumi Ohta,²
Yoshinori Sunaga,² Kiyotaka Sasagawa,¹ and Jun Ohta^{2*}

¹Division of Materials Science, Graduate School of Science and Technology,
Nara Institute of Science and Technology,
8916-5 Takayama, Ikoma, Nara 630-0192, Japan

²Institution of Research Initiative, Nara Institute of Science and Technology,
8916-5 Takayama, Ikoma, Nara 630-0192, Japan

(Received May 20, 2024; accepted June 20, 2024)

Keywords: laser carbonization, electrophysiology, calcium imaging, CMOS, hippocampus

Optical and electrophysiological methods are widely used in neuroscience to study brain activity. Each technique has its own strengths and weaknesses that complement each other to provide a more comprehensive understanding of neuronal activity. To this end, we developed an implantable CMOS image sensor device with an integrated carbon electrode for the simultaneous measurement of fluorescence and extracellular signals. The device is composed of a $450 \times 1660 \mu\text{m}$ CMOS chip and micro-LED secured to a flexible printed circuit substrate. The chip has an imaging surface measuring $900 \times 300 \mu\text{m}^2$, comprising 120×90 pixels recording at 10 frames per second. An absorption filter film was placed on top of the imaging surface to block excitation light. The device was coated with parylene-C for waterproofing and, finally, the coating film was readily turned into carbon electrodes by laser carbonization. We characterized the laser-carbonized electrodes by cyclic voltammetry, electrochemical impedance spectroscopy, and X-ray photoelectron spectroscopy to confirm carbonization. We then demonstrated simultaneous *in vivo* recording of fluorescence and extracellular signals in hippocampus CA1 using the device.

1. Introduction

In vivo investigations of neuron functions are widely conducted with extracellular electrophysiology and optical imaging.⁽¹⁾ Extracellular electrophysiology is the older method but remains the gold standard for observing neuronal activity. This technique involves direct measurement of the electrical activity of neurons and can record at a sub-millisecond resolution. Thus, extracellular recording can record the rapid action potential spikes of individual neurons as well as the collective activity of nearby neurons, referred to as local field potential.⁽²⁾

*Corresponding author: e-mail: ohta@ms.naist.jp
<https://doi.org/10.18494/SAM5145>

However, extracellular recording is limited by its low spatial resolution as direct contact with the electrode is necessary. Furthermore, it is unable to distinguish between different types of neuron as it is just an indiscriminate recording of potential changes.

Optical imaging can mitigate these limitations with its single-cell resolution and cell-specific expression of genetically encoded indicators.⁽³⁾ Fluorescent indicators are typically used in optical imaging as proxy for neuronal activity by determining fluorescence intensity changes in response to ionic concentration, neurotransmitter release, or membrane voltage. Furthermore, many neurons with known localizations can be monitored at the same time, enabling network dynamics studies. However, optical imaging can be slow at a subsecond resolution owing to the indicators' binding kinetics. Additionally, these techniques typically require a fluorescence microscope that immobilizes a mouse to the instrument.

Freely moving mouse experiments have been demonstrated with miniaturized fluorescence microscopes and implantable CMOS image sensors (ICISs).⁽⁴⁾ Owing to the compact and lightweight design of ICISs, device implantations are significantly less invasive, and more naturalistic behavior can be observed.⁽⁵⁾ Moreover, multiregion observations have been conducted through dual-device implantation⁽⁶⁾ or integration with 1⁽⁷⁾ or 2⁽⁸⁾ microdialysis probes. Another advantage of ICISs is the ease of integrating other brain sensing techniques such as fast-scan cyclic voltammetry⁽⁹⁾ and extracellular electrophysiology.^(10,11)

In this paper, we discuss the development of an ICIS with an extracellular electrophysiology recording function. While the integration of ICIS with extracellular electrophysiology has already been reported, this new design significantly streamlines the process. Unlike the approach of Naganuma *et al.*⁽¹⁰⁾ where the electrophysiological recording and imaging components were in separate flexible printed circuits (FPCs), this design incorporates the electrodes in the CMOS chip itself. There is also no need for a separate implantation for the excitation light source⁽¹¹⁾ as the light source is a micro-LED integrated into the device. Lastly, the electrodes were not fabricated by a complicated process such as ball bonding⁽¹¹⁾ but, rather, by a facile carbonization process using a laser. Carbon deposition by a laser provides advantages such as low processing temperature and localized carbonization, minimizing substrate damage, which is very important when the substrate is an electronic chip. Additionally, we used the waterproofing polymer coating as the carbon source, thus serving two purposes at once, further simplifying the fabrication process. Furthermore, carbon electrodes have proven to be more biocompatible and safe than traditional noble metals and exhibit a relatively high electrical conductivity.⁽¹²⁾ The carbonization process was optimized with a Nd:YAG laser in ambient atmosphere and temperature. We characterized the laser-carbonized electrodes by cyclic voltammetry (CV), electrochemical impedance spectroscopy (EIS), and X-ray photoelectron spectroscopy (XPS). We demonstrated the utility of this device by recording hippocampus CA1 activity after the electrical stimulation of hippocampus CA3.

2. Data, Materials, and Methods

2.1 Laser carbonization

Laser carbonization was first performed on flexible gold electrodes for optimization. Gold electrodes were coated with approximately 5 μm of parylene-C (SCS Labcoter® 2) and then exposed to a 266 nm Nd:YAG laser (Callisto VL-C30RS-GV, TNS Systems). For the optimization, the energy setting of the machine was varied from 150 to 450 and the exposure time was varied from 0 to 90 min at a repetition rate of 3 Hz. Optimal laser power was measured with a photodiode (S130VC, Thorlabs). A schematic of the carbonization process and photographs of the electrodes are shown in Fig. 1.

2.2 Characterization

Electrochemical performance was evaluated by CV and EIS using a potentiostat (PGSTAT 204, Metrohm Japan Ltd., Japan) and a frequency response analyzer (Metrohm Japan Ltd., Japan). CV scans were performed with a potential range of -0.2 to 0.8 V for five continuous sweeps at a sweep rate of 50 mV s^{-1} in 0.1 M solutions of dopamine. EIS was performed using a sinusoidal wave in the frequency range of 1 – 10^5 Hz and an amplitude of 10 mV in a 0.1 M phosphate-buffered saline solution. For these measurements, the working electrode was the laser carbonized electrode, whereas the counter electrode was a platinum plate (size: 2×2 cm) and the reference electrode was Ag|AgCl (D.6.0733.100 J, International Chemistry Co., Ltd., Japan). Chemical composition and bonding were evaluated by XPS (ULVAC-PHI Versa Probe II) using a mono-Al $K\alpha$ source.

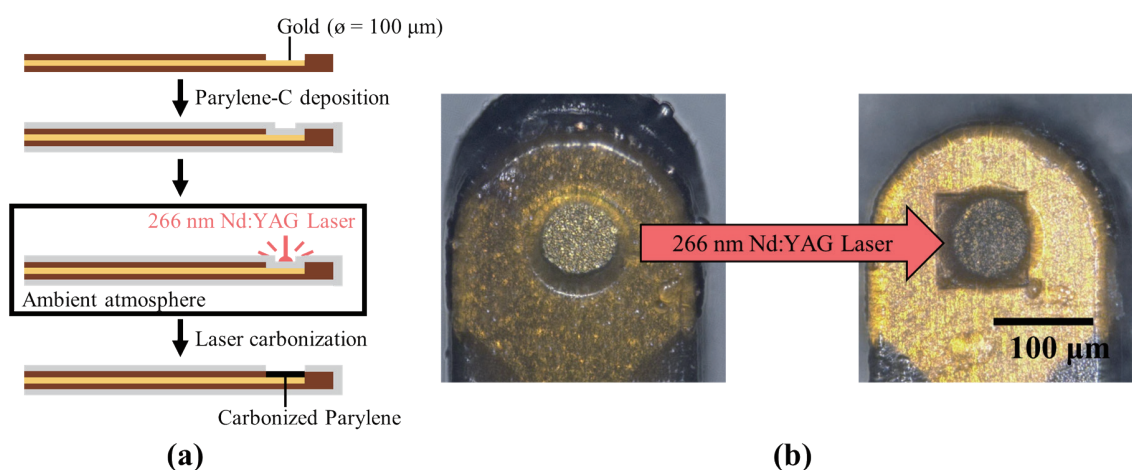


Fig. 1. (Color online) (a) Schematic of laser carbonization process and (b) photographs of parylene-C-coated gold electrodes before and after laser carbonization.

2.3 Electrophysiology–imaging device fabrication

A CMOS imaging chip with an imaging area of 120×40 pixels and an integrated aluminum electrode (size: $100 \times 100 \mu\text{m}^2$) positioned directly above the imaging area was fixed on a polyimide FPC substrate (Taiyo Technorex Co., Ltd., Wakayama, Japan) with epoxy resin (Z-1; Nissin resin, Yokohama, Japan). At the same time, a micro-LED with a center wavelength of 470 nm (ES-VEBCM12A, EPISTAR Corporation, Taiwan) was also immobilized on the FPC with epoxy. Subsequently, the electrical connections of the chip and LED were bonded (7400C-79, West Bond, Anaheim, CA, USA) with aluminum wires (TANAKA Holdings Co., Ltd., Tokyo, Japan) to the FPC. After that, a thin dyed polymer film was positioned on the imaging area and fixed by heating in a vacuum oven for 2 h at $120 \text{ }^\circ\text{C}$. This was the absorption filter for blocking LED light to allow only fluorescent light, which was made by dissolving a yellow dye (Valifast[®] yellow 3150 dye, Orient Chemical Industries, Osaka, Japan) in a photopolymer (Norland Optical Adhesive 63, Cranbury, NJ, USA) film. A 1:1:1 mass solution of Valifast yellow, cyclopentanone, and NOA63 was vigorously mixed with a vortex mixer and then spin-coated on a silicone substrate. The film was heated at $90 \text{ }^\circ\text{C}$ for 30 min and exposed to UV for 30 s for curing. Finally, the absorption filter was patterned with a Nd:YAG laser to match the CMOS imaging area before depositing on the chip. Black resist resin containing a 1:1:1 ratio of SR-3000L, SG-3000L, and SB-3000L (Fujifilm, Tokyo, Japan) was used to close gaps on the sides of the filter before protecting the aluminum wires with epoxy. Lastly, the device was coated with approximately $5 \mu\text{m}$ of parylene-C for waterproofing. This also served as the carbon source for laser carbonization. On the aluminum electrode on top of the imaging area, laser carbonization was performed with a Nd:YAG laser at $1.59 \mu\text{W}$ for 60 min. A photograph of the completed device with a diagram of its components is shown in Fig. 2 with high-magnification images of the imaging area and the laser-carbonized electrode.

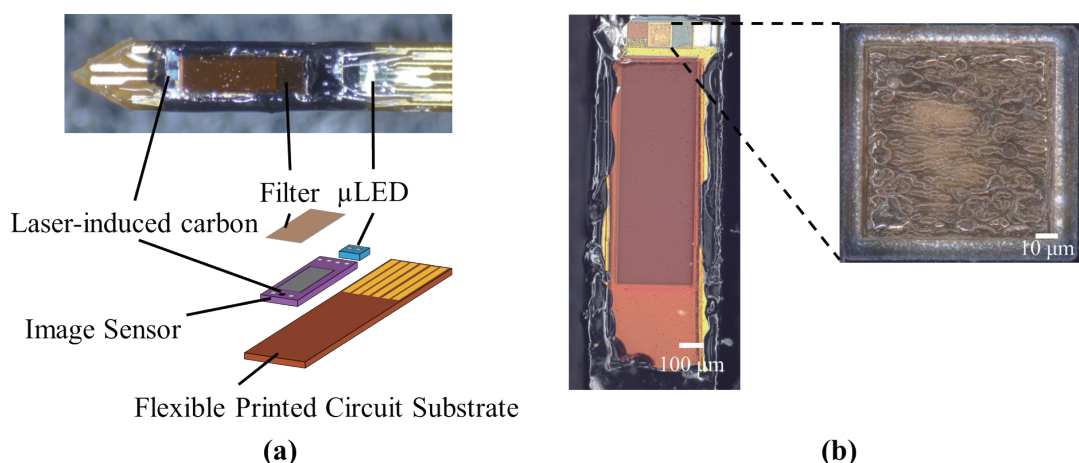


Fig. 2. (Color online) (a) Diagram and photograph of electrophysiology–imaging device and (b) high-magnification images of the device's imaging area and laser-carbonized electrode.

2.4 *In vivo* electrophysiology–imaging experiments

All animal experiments conducted followed the guidelines provided by the Nara Institute of Science and Technology (NAIST) Animal Committee. Transgenic G-CaMP6 mice [strain FVB-Tg (Thy1-GCaMP6)5Shi (RBRC09452, RIKEN)] maintained in the NAIST Animal Facility were used in these experiments. The mice were kept in a 12-h light/dark cycle and given ad libitum access to food and water.

In a typical animal experiment, a mouse was first anesthetized with urethane and its hair was trimmed on the scalp. The mouse was then fixed with an ear bar to a stereotaxic apparatus. Body temperature was maintained with a heating pad underneath the mouse. Afterwards, the scalp was disinfected with chlorhexidine gluconate and incised along the midline to expose the cranium. Burr holes were then drilled for implanting an ICIS to the hippocampus CA1, a bipolar stimulation electrode to hippocampus CA3, and a screw to the brain surface. Next, a screw was tightened on the cranium until contact with the brain to serve as a reference. The ICIS was implanted on the CA1 [−2.2 mm anteroposterior (AP), 1.5 mm mediolateral (ML), 1.8 mm dorsoventral (DV) relative to the bregma] and the stimulation electrode on CA3 (−2.2 mm AP, 2.3 mm ML, 1.8 mm DV relative to the bregma). A schematic of the implantation site is shown in Figs. 3(a) and 3(b). Then, extracellular electrophysiological and calcium imaging signals were recorded for baseline activity until no significant changes occurred. Once the signals from the mouse became stable, tetanic stimulation (50 μ A, 200 Hz duty ratio of 50%, 100 pulses, main interval of 30 s, 4 cycles) of CA3 was performed to induce long-term potentiation in CA1.

To demonstrate simultaneous Ca^{2+} fluorescence imaging and extracellular electrophysiological measurements, known neuronal activity was recorded in the hippocampus. When neurons in CA3 are activated by electrical stimulation, they communicate to those in CA1 via Schaffer collaterals to activate neurons in CA1. The increased electrophysiological activity and Ca^{2+} fluorescence activity from this stimulation are simultaneously recorded by the device's electrode and image sensor, respectively. Furthermore, since the distribution of neurons in the

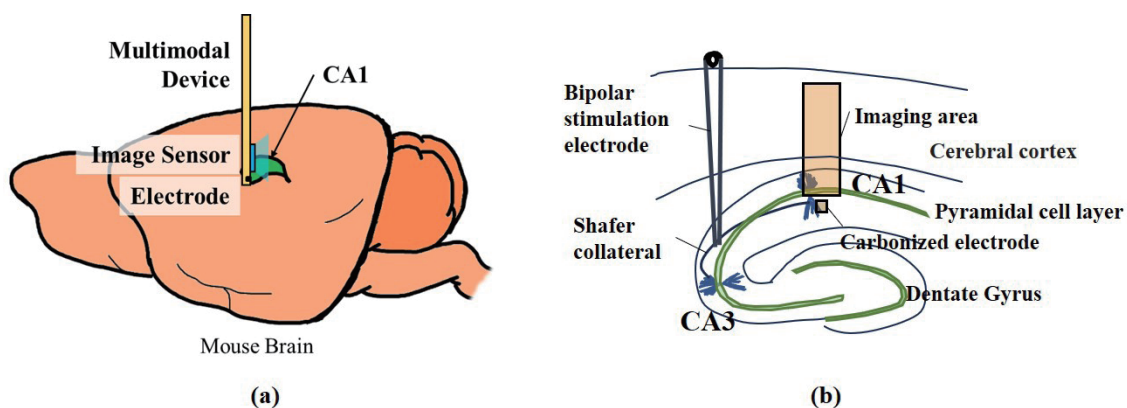


Fig. 3. (Color online) (a) Schematic of the implantation site to hippocampus CA1 in mouse brain and (b) schematic of insertion position of an imaging area, a laser-carbonized electrode, and a bipolar stimulation electrode.

hippocampus is layered, it is easy to show that neuronal activity in CA1 differs depending on the region.

The ICIS was simultaneously connected to custom-built imaging and electrophysiological recording systems. For electrophysiological recording, the device was connected to a preamplifier (SH-MED8, Alpha MED Scientific Inc., Japan) with a 10-fold amplification factor, which was then connected to the main amplifier (SU-MED8, Alpha MED Scientific Inc., Japan) with a 100-fold amplification factor. The main amplifier was equipped with a 60 Hz notch filter and a 100–5000 Hz bandpass filter. The signals input to the main amplifier were recorded using Micro1401 mkII (Cambridge Electronic Design Ltd., UK) at a sampling frequency of 20 kHz at a resolution of 24 bits. For calcium imaging, the ICIS was connected to a custom-built imaging platform named CIS-OS⁽¹³⁾ recording at 10 frames per second.

2.5 Data analysis

A custom-built Python algorithm was developed for determining regions of interest (ROIs) in the ICIS imaging data consisting of a series of adaptive binarization and morphological transformations (Fig. 4).⁽⁸⁾

The start and end of the stimulation procedure were marked in the imaging data. The data was then trimmed into 5 min before the stimulation and 30 min after. These two segments were then concatenated. The frames before stimulation were designated as the baseline, F_0 .

Before ROI selection, each pixel was baselined to $\% \Delta F_i / F_{i,0}$ as expressed in Eq. (1), where $F_{i,t}$ is the fluorescence intensity of the i th pixel at the time point t and $F_{i,0}$ is the average baseline fluorescence of the i th pixel.

$$\% \Delta F_i / F_{i,0} = [(F_{i,t} - F_{i,0}) / F_{i,0}] \times 100\% \quad (1)$$

Adaptive binarization by a Gaussian method was applied to each frame after stimulation. A morphological opening was then used to clean the binarized frames before averaging all the frames. Afterwards, adaptive binarization was performed again and, subsequently, morphological opening. Each shape in the resulting image was designated as an ROI.

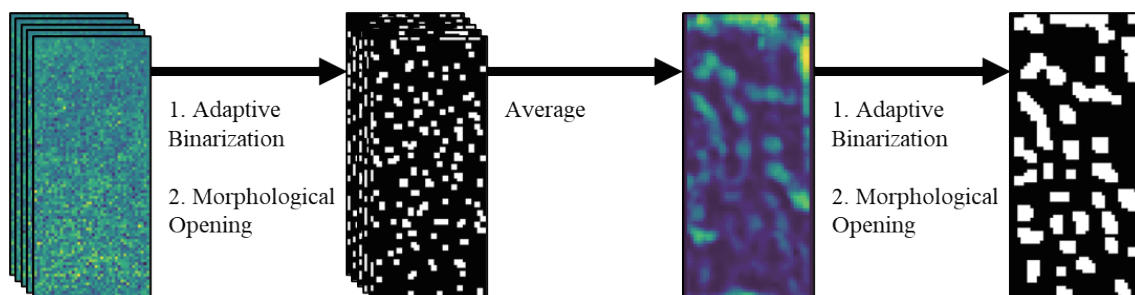


Fig. 4. (Color online) Schematic of ROI selection algorithm using viridis color map (dark green for low values and bright yellow for high values).

After ROI selection, ROI traces were calculated using Eq. (2), where \bar{F}_t is the average fluorescence of all pixels at the time point t in the ROI and F_0 is the average baseline fluorescence of all pixels in the ROI.

$$\% \Delta F / F_0 = [(\bar{F}_t - F_0) / F_0] \times 100\% \quad (2)$$

All data processing was conducted in Python 3.10.6 [<http://www.python.org/> (accessed on 10 October 2023)] with Spyder IDE 5.4.3. Statistical testing was done with SciPy 1.11.3.⁽¹⁴⁾ Morphological image processing and adaptive binarization were performed with scikit-image 0.22.0.⁽¹⁵⁾ Principal component analysis, k-means clustering, and silhouette score calculation were implemented with scikit-learn 1.3.1.⁽¹⁶⁾

3. Results

3.1 Optimization of laser power and duration

We first investigated the effects of laser power and exposure time on the electrochemical properties of the laser-carbonized electrodes using cyclic voltammetry. Figure 5 shows the

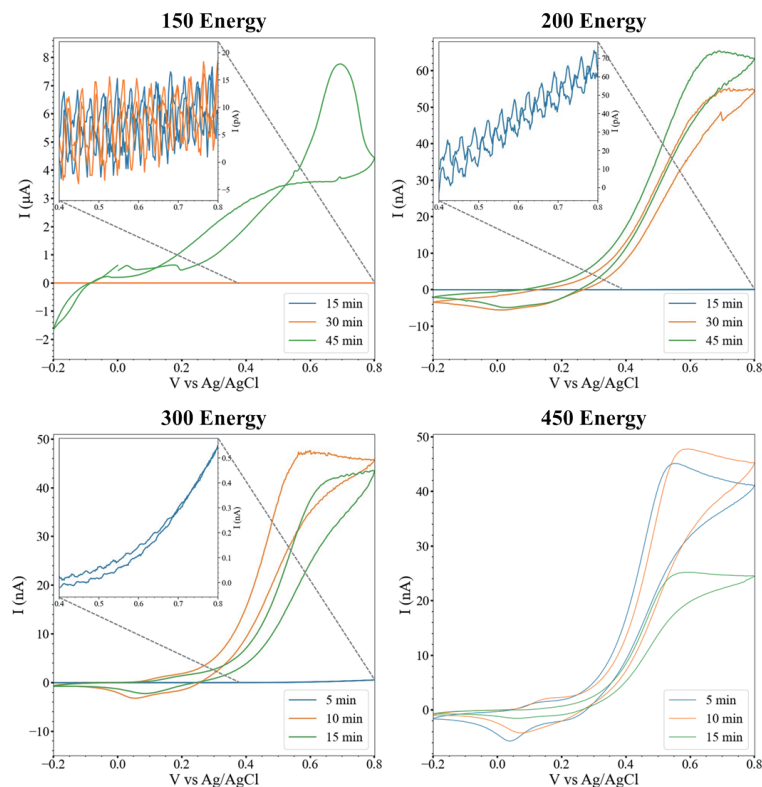
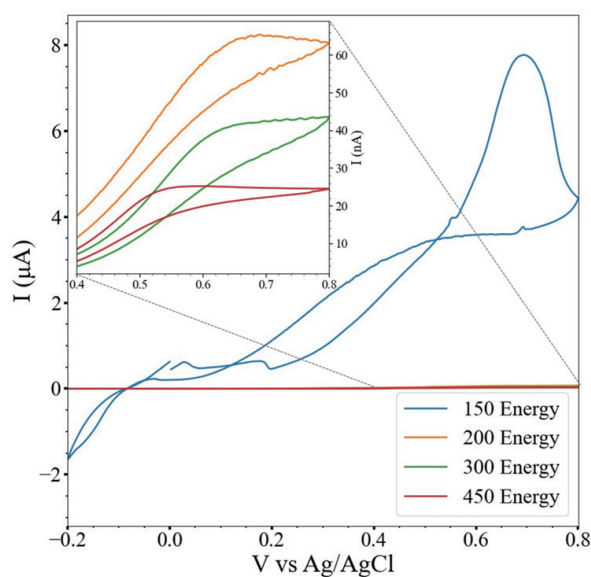


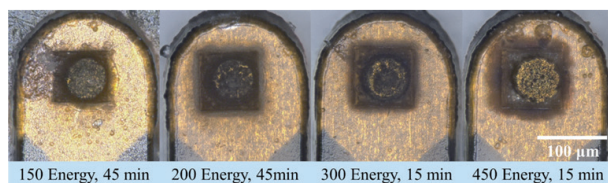
Fig. 5. (Color online) Cyclic voltammogram of laser-carbonized electrodes at different laser energy settings and exposure times.

voltammograms of the laser-carbonized electrodes at different energy settings and exposure time. At a 150-energy setting, 45 min of exposure was necessary to fully carbonize the polymer since only noise level current was detected with electrodes that were laser-carbonized for 15 and 30 min. The required duration decreased to 30 min when a 200-energy setting was used. When a 300-energy setting was used, the electrodes were already conductive with only 10 min of laser exposure. At a 450-energy setting, the electrodes were conductive even at 5 min of laser exposure.

However, faradaic current was only observed when using a 150-energy setting as shown in Fig. 6(a). This indicates that the electrodes produced using lasers with higher energy settings (200, 300 and 450) are not electrochemically active. This can be explained by the decreased carbon coverage as shown in Fig. 6(b). More of the underlying gold electrode is exposed when using higher energy settings. Very little carbon can be observed for electrodes subjected to the highest energy setting of 450 energy for 15 min. Hence, the optimal energy setting is 150, which was measured to have a laser power of $1.59 \mu\text{W}$. This energy setting was used for all other laser carbonizations.



(a)



(b)

Fig. 6. (Color online) (a) Cyclic voltammogram and (b) photographs of laser-carbonized electrodes at different laser energy settings and exposure times.

We then investigated the effects of exposure time on the electrochemical properties of the laser-carbonized electrodes by EIS. Figure 7 shows that at a laser power of $1.59 \mu\text{W}$, the minimum exposure time required was 45 min. At 15 and 30 min of exposure, the spectrum is equivalent to those of samples not exposed to laser, indicating that the insulating polymer coating has not been fully carbonized. The impedance decreases further with 60 min of exposure. More importantly, the impedance of this electrode is lower than that of the uncoated gold electrode. This improved impedance could indicate that the laser-carbonized electrode has a larger surface area since the electrode areas are the same. There are no further impedance improvements with longer exposure time.

3.2 Elemental composition

The laser-induced carbon and original polymer were characterized by XPS to determine their elemental composition (Fig. 8). A decreased C1s peak intensity was observed in laser-induced carbon compared with parylene-C, indicating a decreased proportion of carbon in the sample. This is corroborated by the higher O1s peak of the laser-induced carbon. This means that parylene-C was successfully carbonized leading to more oxygen functional groups since carbon

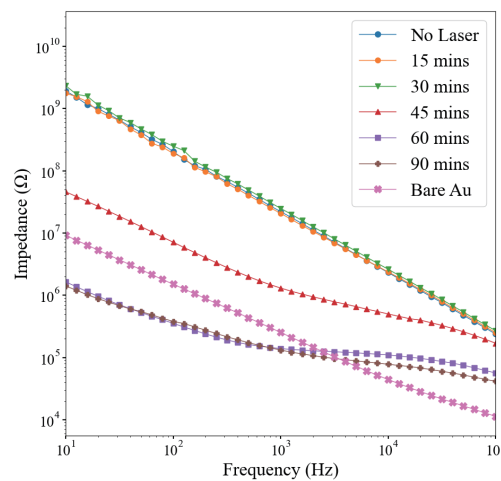


Fig. 7. (Color online) Changes in EIS properties of laser-induced carbon with increasing laser exposure time.

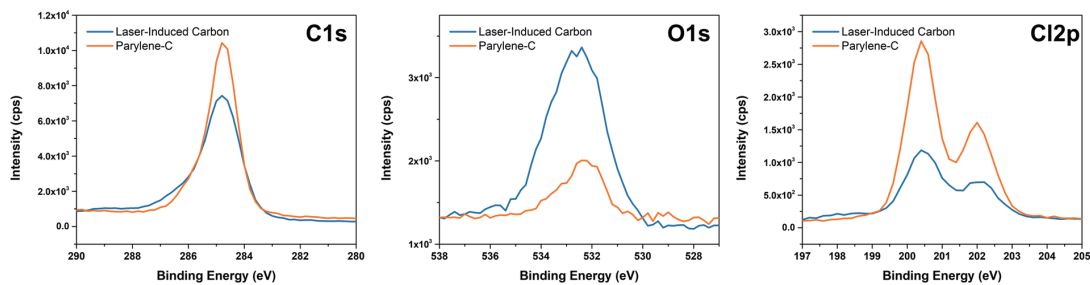


Fig. 8. (Color online) Narrow-scan XPS C1s, O1s, and Cl2p peaks of laser-induced carbon and parylene-C.

materials are typically terminated by oxygen functional groups.⁽¹⁷⁾ Additionally, we deconvoluted the C1s and O1s peaks to determine the chemical bonds present in these materials. Binding energies of approximately 285, 286, and 291 eV correspond to C–C, C–O, and π - π^* peaks, respectively.^(17–19) The C1s peak of laser-induced carbon contained 84.6% C–C bonds and 15.4% C–O bonds, which are different from the original polymer, parylene-C, which contained 91.8% C–C bonds and 8.2% C–O bonds (Fig. 9). Furthermore, π - π^* bonds were detected in parylene-C from its aromatic ring that was not present in the laser-induced carbon. In the O1s peak of laser-induced carbon, O–C, O–H, and O=C comprised 47.7%, 29.6%, and 22.7%, while the values were 62.8%, 19.0%, and 18.2% for parylene-C, respectively. This further confirms the carbonization of parylene-C as the abundance of O–H and O=C bonds increases in the carbon sample. Finally, a decrease in Cl2p intensity was also observed in the laser-induced carbon compared with parylene-C (Fig. 8). Taken together, these results confirm the laser-induced carbonization of parylene-C.

3.3 Detection of brain activity with electrophysiology–imaging device

We performed simultaneous *in vivo* recording of electrophysiological and optical signals with the implantable electrophysiology–imaging device. The device was implanted in hippocampal CA1 to observe localized activity due to the layered structure of the hippocampus. The bipolar stimulating electrode was implanted in the CA3 for tetanic stimulation and to induce long-term potentiation of the CA1.⁽²⁰⁾ Hippocampal CA1 activity was recorded following the tetanic stimulation of the CA3. Figure 10(a) shows the average frame of calcium imaging data every 5

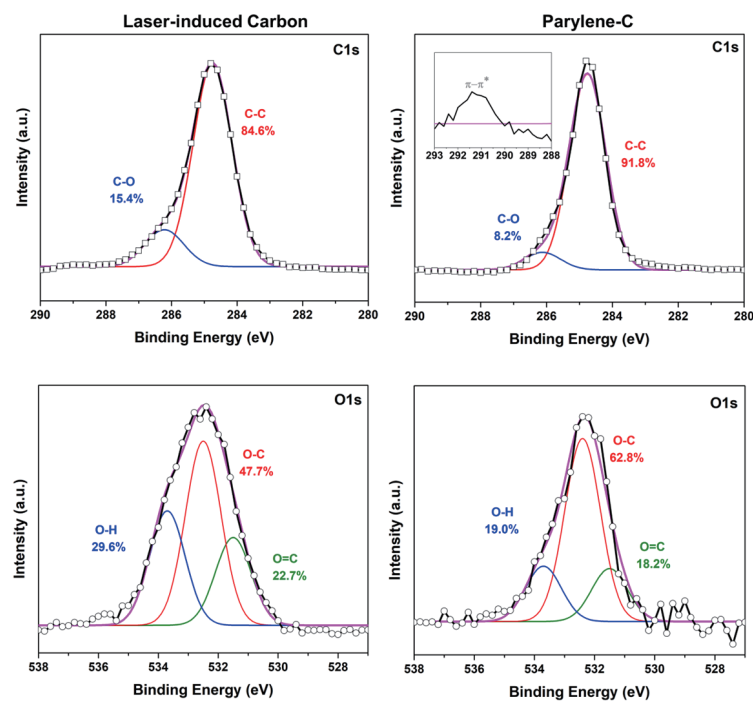


Fig. 9. (Color online) Deconvolution of XPS C1s and O1s peaks of laser-induced carbon and parylene-C.

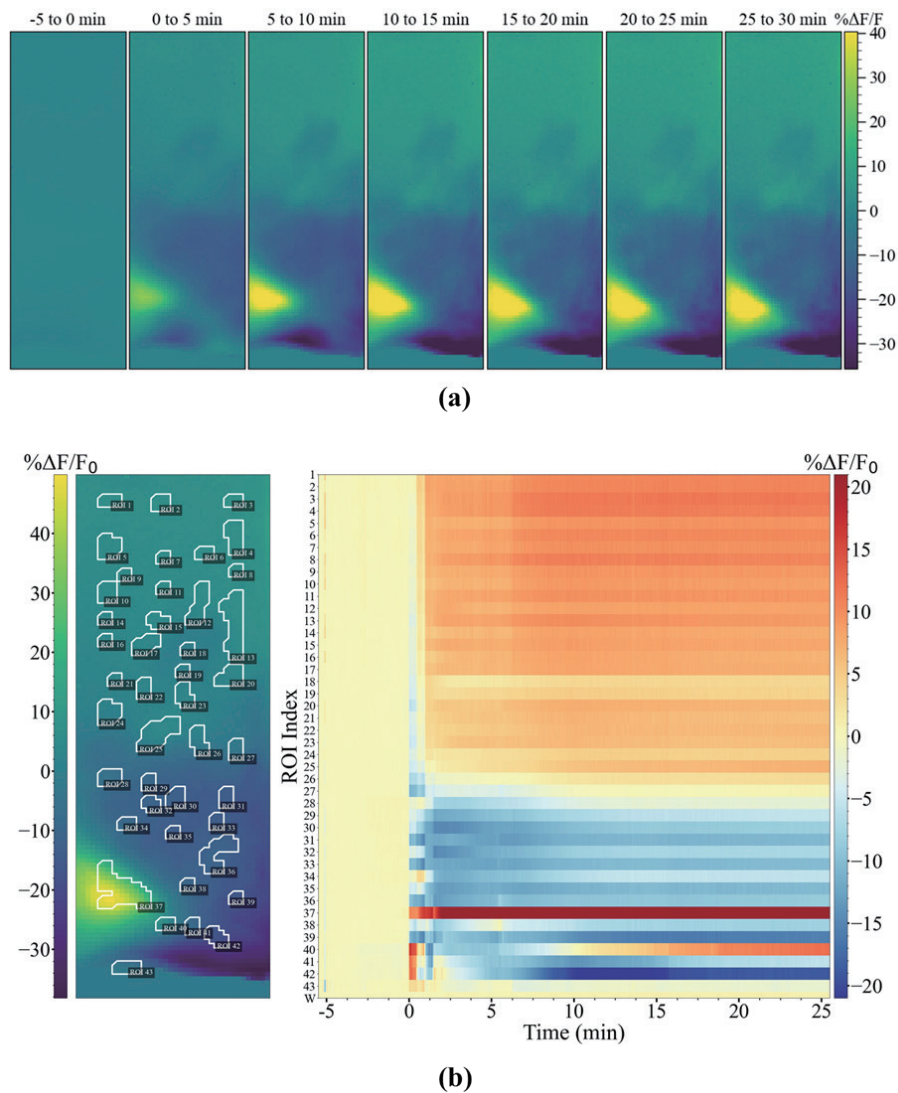


Fig. 10. (Color online) (a) Average hippocampal CA1 fluorescence activity image every 5 min and (b) average fluorescence activity of each ROI displayed in pseudocolor.

min. Increasing local intensity is observed in the bottom left corner of the frame, indicating an elevated CA1 fluorescence activity. A custom-built algorithm was used to identify ROIs in the video to avoid subjective bias. The average fluorescence activity of each ROI is shown in Fig. 10(b). The top part of the image showed increasing activity (until ROI 27), while ROIs 28 to 38 (except 37) showed a trend of decreasing activity. This difference in fluorescence activity was expected given that different brain regions were recorded with the image sensor. As shown in Fig. 3(b), the top part of the image sensor is not in the CA1, whereas the bottom part is. Therefore, the activity patterns for these different brain regions should be different. This also demonstrates the capability of the image sensor to capture brain activity in different layers of the brain.

The extracellular recording data was analyzed by calculating the change in FFT amplitude of different frequency bands from baseline levels (Fig. 11). A considerable drop in FFT amplitude is observed in all frequency bands except for the ripple and δ bands after stimulation. This is similar to the progression of the fluorescence signal of the ROI 42 in the Ca^{2+} imaging data. On the other hand, the increase in ripple band activity could be correlated with the increase in the activity of ROI 37. These results suggest that the implantable electrophysiology–imaging sensor can simultaneously record calcium imaging and extracellular electrophysiological signals.

4. Discussion

We developed an ICIS with an integrated electrophysiological recording function by incorporating a carbon electrode prepared using a facile carbonization technique. The method

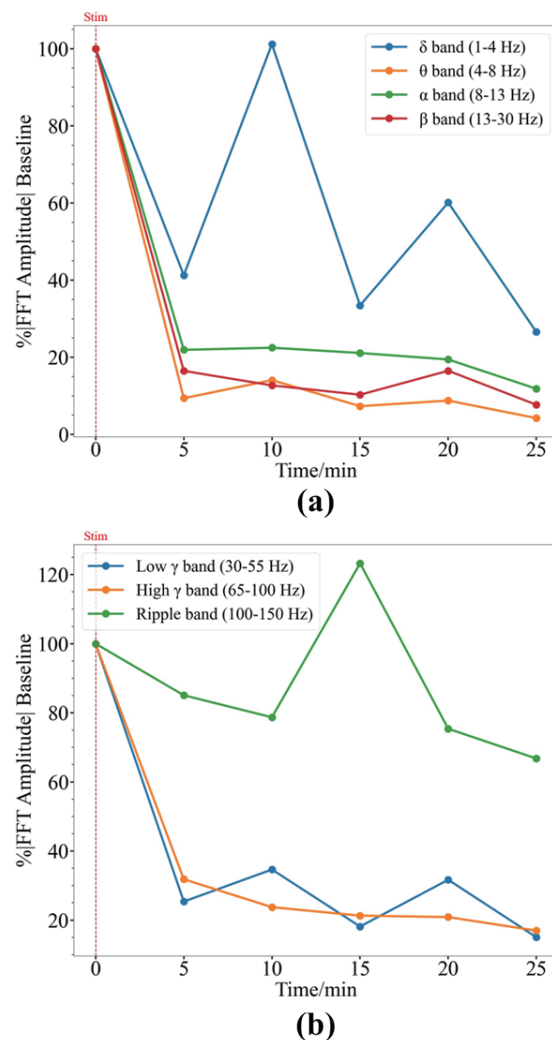


Fig. 11. (Color online) Changes in the FFT amplitude from the baseline levels of (a) δ , θ , α , and β , and (b) low γ , high γ , and ripple bands in the extracellular recording.

does not require complicated steps and significantly simplifies the device assembly process by utilizing the already present waterproofing film on the device. This is also the first ICIS to streamline simultaneous electrophysiology–imaging experiments without needing a hybrid design⁽¹⁰⁾ or a separate light source.⁽¹¹⁾

We measured the cyclic voltammograms of the laser-carbonized electrodes to evaluate the electrochemical activity. Since our method uses a 266 nm Nd:YAG UV laser instead of a visible or infrared laser, it was important to optimize the carbonization process. We found the optimal exposure power to be 1.59 μW , which is significantly lower than those for typical laser carbonizations with an infrared laser reported in the literature.^(21–24) Carbonization with a laser at a power higher than 1.59 μW opened the electrodes faster, as indicated by the above noise-level voltammograms (Fig. 5). However, these electrodes showed no electrochemical oxidation capability [Fig. 6(a)] and decreased carbonization [Fig. 6(b)], which was indicated by the increase in the proportion of gold on the electrode surface. These results are important for other future neural applications of these carbon electrodes in neuronal recording, such as fast-scan cyclic voltammetry.

We then used EIS to assess the suitability of the electrodes for extracellular recording. We found the optimal exposure time to be 60 min considering that the electrode exhibits 139 k Ω of impedance at 1 kHz, which is sufficiently low for extracellular electrophysiological recording.⁽²⁵⁾ The electrode is already conductive after 45 min but the impedance is still insufficient at 1.3 M Ω .

We confirmed the carbonization by comparing the X-ray photoelectron spectra of the laser-carbonized electrode and the carbon source polymer, parylene-C. The C1s spectrum of parylene-C shows the typical π – π^* peak observed for this polymer from the conjugated benzene ring (Fig. 8).⁽¹⁹⁾ This peak is not present in the C1s spectrum of laser-carbonized electrode but instead contains carbonyl groups and a larger proportion of C–O groups, which is typical of carbon samples.⁽¹⁷⁾ These results indicate the carbonization of parylene-C, which is also validated by the presence of more functional groups in the O1s peak of the laser-carbonized electrode compared with that of the parylene-C.^(26,27)

The optimized laser carbonization process was then used to integrate the electrophysiological recording function into an ICIS. To detect observable brain signals, the device implanted in hippocampus CA1 and then CA3 was electrostimulated with a bipolar electrode. The calcium imaging and extracellular activity of CA1 were then simultaneously recorded. Figures 10 and 11 show the changes in the calcium imaging and extracellular electrophysiology signals, respectively. Similarities between calcium imaging ROIs and extracellular recording frequency bands were observed. The low correlation value could be due to the distance of the electrode from the neuron that is in the frame of the image sensor. Extracellular recording is a contact technique that can record up to a distance of approximately only 1000 μm away from the electrode.⁽²⁾ In addition, more animal experiments need to be conducted in the future to confirm the physiological significance of the obtained results, such as the decreasing power of the electrophysiological recording after stimulation and the incredibly high $\%\Delta F/F_0$ of one ROI.

The implantable electrophysiology–imaging sensor enables for the simultaneous measurement of optical and electrophysiological signals without the need for two devices,

minimizing implantation injury and unnecessary movement restrictions. The device can be improved in the future to include a multiple-electrode array to enable spike sorting or to chemically functionalize the electrode to enable more sensing modes such as fast-scan cyclic voltammetry.

5. Conclusions

In this study, we developed a streamlined implantable electrophysiology–imaging sensor that does not use any hybrid elements. We achieved this by utilizing the waterproofing coating of the device for locally producing carbon with a laser on the CMOS chip electrode. This was a simple and very efficient method to make carbon electrodes since implantable imaging devices are typically coated with parylene-C as part of the fabrication process. We optimized the laser carbonization process at ambient atmosphere and found that this carbonization condition favors carbon formation at a lower laser power, as a higher laser power resulted in less carbonization. We confirmed the carbonization by XPS. Additionally, only a low-power laser produced electrochemically active carbon, which can be useful for future integrations with other brain sensing techniques. We then performed *in vivo* experiments with the ICIS with an integrated electrophysiological recording function to confirm that the device can simultaneously record extracellular electrophysiological and fluorescence signals.

The facile carbonization process allows for the easy fabrication of multiple electrodes, which will be helpful in the future for spike sorting applications. Furthermore, we have the freedom to design the CMOS chip and adjust the electrode position, number, and size; we can even place electrodes within the imaging area. The electrode can also be functionalized by using different waterproofing polymer coatings to enhance sensitivity for electrochemical brain sensing techniques.

Acknowledgments

This work was supported by JSPS KAKENHI (JP23H05450) and the VLSI Design and Education Center, University of Tokyo, in collaboration with Cadence Design Systems, Inc.

References

- 1 C. M. Lewis, A. Hoffmann, and F. Helmchen: *Neurophotonics* **11** (2023) 033403. <https://doi.org/10.1117/1.nph.11.3.033403>
- 2 B. Pesaran, M. Vinck, G. T. Einevoll, A. Sirota, P. Fries, M. Siegel, W. Truccolo, C. E. Schroeder, and R. Srinivasan: *Nat. Neurosci.* **21** (2018) 903. <https://doi.org/10.1038/s41593-018-0171-8>
- 3 Y. Zhang and L. L. Looger: *J. Physiol.* **602** (2024) 1595. <https://doi.org/10.1113/JP283832>
- 4 Y. Sunaga, Y. Ohta, Y. M. Akay, J. Ohta, and M. Akay: *IEEE Access* **8** (2020) 68013. <https://doi.org/10.1109/ACCESS.2020.2985705>
- 5 J. Ohta, Y. Ohta, H. Takehara, T. Noda, K. Sasagawa, T. Tokuda, M. Haruta, T. Kobayashi, Y. M. Akay, and M. Akay: *Proc. IEEE* **105** (2017) 158. <https://doi.org/10.1109/JPROC.2016.2585585>
- 6 R. Rebusi, J. P. Olorocisimo, J. Briones, Y. Ohta, M. Haruta, H. Takehara, H. Tashiro, K. Sasagawa, and J. Ohta: *Front. Neurosci.* **15** (2021) 1. <https://doi.org/10.3389/fnins.2021.667708>
- 7 Y. Sunaga, Y. Ohta, T. E. Murakami, Y. M. Akay, J. Ohta, and M. Akay: *IEEE Access* **9** (2021) 55871. <https://doi.org/10.1109/ACCESS.2021.3071961>

- 8 L. Akbar, V. C. G. Castillo, J. P. Olorocisimo, Y. Ohta, M. Kawahara, H. Takehara, M. Haruta, H. Tashiro, K. Sasagawa, M. Ohsawa, Y. M. Akay, M. Akay, and J. Ohta: *Int. J. Mol. Sci.* **24** (2023) 6654. <https://doi.org/10.3390/ijms24076654>
- 9 R. Siwadamrongpong, N. Sato, K. Sugie, Y. Ohta, M. Haruta, H. Takehara, H. Tashiro, K. Sasagawa, and J. Ohta: *Proc. 2022 44th Annu. Int. Conf. IEEE Engineering in Medicine & Biology Society (EMBC) Glasgow (IEEE, 2022)* 4864–4867. <https://doi.org/10.1109/EMBC48229.2022.9871016>
- 10 K. Naganuma, Y. Ohta, T. E. Murakami, R. Okada, M. C. Guinto, H. Takehara, M. Haruta, H. Tashiro, K. Sasagawa, Y. Sunaga, Y. M. Akay, M. Akay, and J. Ohta: *Sens. Mater.* **34** (2022) 1561. <https://doi.org/10.18494/SAM3710>
- 11 K. Sugie, K. Sasagawa, R. Okada, Y. Ohta, H. Takehara, M. Haruta, H. Tashiro, and J. Ohta: *Sens. Mater.* **35** (2023) 3173. <https://doi.org/10.18494/SAM4264>
- 12 M. Devi, M. Vomero, E. Fuhrer, E. Castagnola, C. Gueli, S. Nimbalkar, M. Hirabayashi, S. Kassegne, T. Stieglitz, and S. Sharma: *J. Neural Eng.* **18** (2021) 041007. <https://doi.org/10.1088/1741-2552/ac1e45>
- 13 A. Ganaway, K. Tatsuta, V. C. G. Castillo, R. Okada, Y. Sunaga, Y. Ohta, J. Ohta, M. Ohsawa, M. Akay, and Y. M. Akay: *Int. J. Mol. Sci.* **24** (2023) 16303. <https://doi.org/10.3390/ijms242216303>
- 14 P. Virtanen, R. Gommers, T. E. Oliphant, M. Haberland, T. Reddy, D. Cournapeau, E. Burovski, P. Peterson, W. Weckesser, J. Bright, S. J. van der Walt, M. Brett, J. Wilson, K. J. Millman, N. Mayorov, A. R. J. Nelson, E. Jones, R. Kern, E. Larson, C. J. Carey, Í. Polat, Y. Feng, E. W. Moore, J. VanderPlas, D. Laxalde, J. Perktold, R. Cimrman, I. Henriksen, E. A. Quintero, C. R. Harris, A. M. Archibald, A. H. Ribeiro, F. Pedregosa, P. van Mulbregt, A. Vijaykumar, A. Pietro Bardelli, A. Rothberg, A. Hilboll, A. Kloeckner, A. Scopatz, A. Lee, A. Rokem, C. N. Woods, C. Fulton, C. Masson, C. Häggström, C. Fitzgerald, D. A. Nicholson, D. R. Hagen, D. V. Pasechnik, E. Olivetti, E. Martin, E. Wieser, F. Silva, F. Lenders, F. Wilhelm, G. Young, G. A. Price, G. L. Ingold, G. E. Allen, G. R. Lee, H. Audren, I. Probst, J. P. Dietrich, J. Silterra, J. T. Webber, J. Slavič, J. Nothman, J. Buchner, J. Kulick, J. L. Schönberger, J. V. de Miranda Cardoso, J. Reimer, J. Harrington, J. L. C. Rodriguez, J. Nunez-Iglesias, J. Kuczynski, K. Tritz, M. Thoma, M. Newville, M. Kümmerer, M. Bolingbroke, M. Tartre, M. Pak, N. J. Smith, N. Nowaczyk, N. Shebanov, O. Pavlyk, P. A. Brodtkorb, P. Lee, R. T. McGibbon, R. Feldbauer, S. Lewis, S. Tygier, S. Sievert, S. Vigna, S. Peterson, S. More, T. Pudlik, T. Oshima, T. J. Pingel, T. P. Robitaille, T. Spura, T. R. Jones, T. Cera, T. Leslie, T. Zito, T. Krauss, U. Upadhyay, Y. O. Halchenko, and Y. Vázquez-Baeza: *Nat. Methods* **17** (2020) 261. <https://doi.org/10.1038/s41592-019-0686-2>
- 15 S. van der Walt, J. L. Schönberger, S. Schönberger, J. Nunez-Iglesias, F. Ois Boulogne, J. D. Warner, and N. Yager: *PeerJ* **2** (2014) e453. <https://doi.org/10.7717/peerj.453>
- 16 F. Pedregosa, G. Varoquaux, A. Gramfort, V. Michel, B. Thirion, O. Grisel, M. Blondel, P. Prettenhofer, R. Weiss, V. Dubourg, A. Gramfort, B. Thirion, O. Grisel, V. Dubourg, J. Vanderplas, A. Passos, D. Cournapeau, M. Brucher, M. Perrot, and É. Duchesnay: *J. Mach. Learn. Res.* **12** (2011) 2825.
- 17 D. J. Morgan: *C J. Carbon Res.* **7** (2021) 51. <https://doi.org/10.3390/c7030051>
- 18 P. C. Bandara, J. Peña-Bahamonde, and D. F. Rodrigues: *Sci. Rep.* **10** (2020) 9237. <https://doi.org/10.1038/s41598-020-65534-8>
- 19 S. Gholizadeh, D. M. Lincoln, Z. Allahyari, L. P. Widom, R. N. Carter, and T. R. Gaborski: *Sci. Rep.* **13** (2023) 4262. <https://doi.org/10.1038/s41598-023-31305-4>
- 20 Y. V. Dobryakova, M. Yu. Stepanichev, V. A. Markevich, and A. P. Bolshakov: *Int. J. Neurosci.* **132** (2022) 490. <https://doi.org/10.1080/00207454.2020.1822834>
- 21 Oliveira, J. S. Ordonez, D. A. Vajari, M. Eickenscheidt, and T. Stieglitz: *Eur. J. Transl. Myology* **26** (2016). <https://doi.org/10.4081/ejtm.2016.6062>
- 22 M. Vomero, A. Oliveira, D. Ashouri, M. Eickenscheidt, and T. Stieglitz: *Sci. Rep.* **8** (2018) 1. <https://doi.org/10.1038/s41598-018-33083-w>
- 23 M. Burke, C. Larrigy, E. Vaughan, G. Paterakis, L. Sygellou, A. J. Quinn, G. Herzog, C. Galiotis, and D. Iacopino: *ACS Omega* **5** (2020) 1540. <https://doi.org/10.1021/acsomega.9b03418>
- 24 H. Wang, S. Delacroix, O. Osswald, M. Anderson, T. Heil, E. Lepre, N. Lopez-Salas, R. B. Kaner, B. Smarsly, and V. Strauss: *Carbon N. Y.* **176** (2021) 500. <https://doi.org/10.1016/j.carbon.2021.01.145>
- 25 J. P. Neto, P. Baião, G. Lopes, J. Frazão, J. Nogueira, E. Fortunato, P. Barquinha, and A. R. Kampff: *Front. Neurosci.* **12** (2018). <https://doi.org/10.3389/fnins.2018.00715>
- 26 Y. C. G. Kwan, G. M. Ng, and C. H. A. Huan: *Thin Solid Films* **590** (2015) 40 <https://doi.org/10.1016/j.tsf.2015.07.051>
- 27 G. Simões Dos Reis, C. Mayandi Subramaniam, A. D. Cárdenas, S. H. Larsson, M. Thyrel, U. Lassi, and F. García-Alvarado: *ACS Omega* **7** (2022) 42570. <https://doi.org/10.1021/acsomega.2c06054>

About the Authors



Virgil Christian G. Castillo received his B.S. degree in chemistry from Xavier University – Ateneo de Cagayan, Philippines, in 2014 and his M.S. degree in chemistry from Ateneo de Manila University, Philippines, in 2019. He is currently pursuing his Ph.D. degree at Nara Institute of Science and Technology. His research interests include bioengineering and sensors. (castillo.virgil_christian.cr3@ms.naist.jp)



Kuang-Chih Tso received his B.S degree from National Chiao Tung University (Department of Applied Chemistry, 2015), M.S. degree from National Chiao Tung University (Graduate Degree Program of Science and Technology of Accelerator Light Source, 2017), and Ph.D. degree under a dual-degree program from Nara Institute of Science and Technology and National Yang Ming Chiao Tung University (2023). Currently, he is a postdoctoral researcher in the Research Laboratory on Next-Generation Biomedical Engineering of Nara Institute of Science and Technology. His major research interests are bio-electrode fabrication, artificial retina device development, and atomic/microstructure analyses from materials to devices. (tso.kuang_chih@ms.naist.jp)



Ryoma Okada received his B.E. degree in electrical and electronic engineering from Shizuoka University, Shizuoka, Japan, and his M.E. degree from Nara Institute of Science and Technology (NAIST), Nara, Japan. He is currently pursuing his Ph.D. degree at the Photonic Device Science Laboratory in NAIST. His current research interests are polarization image sensors and electromagnetic field imaging. (okada.ryoma.on9@ms.naist.jp)



Yasumi Ohta received her B.S. degree in physics from Nara Women's University in 1984. She enrolled in the Faculty of Science at Kyoto University in 2004 and switched to a master's program at the Graduate School of Science, Kyoto University, in 2006. She received her M.S. and Ph.D. degrees in biophysics from Kyoto University, Kyoto, Japan, in 2008 and 2011, respectively. From 1984 to 1986, she worked at Mitsubishi Electric Corp. in Hyogo, Japan. In 2011, she joined Nara Institute of Science and Technology (NAIST) in Nara, Japan, as a postdoctoral fellow. Her research interests include implantable bioimaging CMOS sensors and neuroscience. (ohtay@ms.naist.jp)



Yoshinori Sunaga received his B.E. degree from Chiba University, Japan, in 2012 and M.E. and Ph.D. degrees from the Graduate School of Materials Science, Nara Institute of Science and Technology (NAIST), Japan, in 2014 and 2017, respectively. In 2017, he joined NAIST as a postdoctoral fellow and began collaborative research between NAIST and the University of Houston. In 2019, he joined the University of Houston as a postdoctoral fellow. He joined NAIST as a postdoctoral fellow in 2022 and was specially appointed as an assistant professor in 2023. He is interested in developing novel devices for observing and assessing brain activity in animals to reveal new brain mechanisms. (sunaga.yoshinori@ms.naist.jp)



Kiyotaka Sasagawa received his B.S. degree from Kyoto University in 1999 and his M.E. and Ph.D. degrees in materials science from NAIST, Japan, in 2001 and 2004, respectively. Subsequently, he became a researcher at the National Institute of Information and Communications Technology in Tokyo, Japan. In 2008, he joined NAIST as an assistant professor and became an associate professor in 2019. His research interests include bioimaging, biosensing, and electromagnetic field imaging. (sasagawa@ms.naist.jp)



Jun Ohta received his B.E., M.E., and Dr. Eng. degrees in applied physics from The University of Tokyo, Japan, in 1981, 1983, and 1992, respectively. In 1983, he joined Mitsubishi Electric Corporation, Hyogo, Japan. From 1992 to 1993, he was a visiting scientist at the Optoelectronics Computing Systems Center at the University of Colorado, Boulder. In 1998, he joined the Graduate School of Materials Science, Nara Institute of Science and Technology (NAIST), Nara, Japan, as an associate professor, and was appointed as a professor in 2004. His current research interests include smart CMOS image sensors for biomedical applications and retinal prosthetic devices. He is a Fellow of IEEE, the Japan Society of Applied Physics, and the Institute of Image, Information, and Television Engineers. (ohta@ms.naist.jp)